

## Article

# Phase Transition and Switchable Dielectric Properties of a Three-Dimensional Hydrogen-Bonding Framework Based on Cobalt (III), *o*-Bromoaniline, and 18-Crown-6

Hong-Zhi Hu <sup>1,2</sup>, Yi-Bo Yan <sup>1,2</sup>, Na Wang <sup>1</sup>, Abuduheni Adila <sup>1</sup>, Yang Liu <sup>1,3,\*</sup> and Zun-Qi Liu <sup>1,3,\*</sup>

<sup>1</sup> Chemistry and Chemical Engineering College, Xinjiang Agricultural University, Ürümqi 830052, China; huhongzhi305@163.com (H.-Z.H.); yanyibo2022@163.com (Y.-B.Y.); 15310053737@163.com (N.W.); 17799751675@163.com (A.A.)

<sup>2</sup> College of Mechanical and Electrical Engineering, Xinjiang Agricultural University, Ürümqi 830052, China

<sup>3</sup> Xinjiang Sub-Center, National Engineering Research Center of Novel Equipment for Polymer Processing, Guangzhou 510641, China

\* Correspondence: ly2021@xjau.edu.cn (Y.L.); lzbq@xjau.edu.cn (Z.-Q.L.); Tel.: +86-991-876-2118 (Z.-Q.L.)

**Abstract:** The organic–inorganic hybrid compound, (*o*-BrAH)[H<sub>2</sub>Co(CN)<sub>6</sub>]<sub>0.5</sub>·(18-crown-6)<sub>0.5</sub>·H<sub>2</sub>O, was synthesized and characterized by variable-temperature X-ray diffraction, single-crystal diffraction, infrared spectroscopy, elemental analysis, thermogravimetric analysis, differential scanning calorimetry, and dielectric measurements. Single-crystal X-ray diffraction revealed a three-dimensional cage-like structure formed through the hydrogen bonds of cobalt hexacyanide, supermolecular cations, and water molecules. Temperature variation triggered an abrupt change in the cage structure and simultaneously caused dynamic oscillation of the supramolecules within the framework of [Co(CN)<sub>6</sub>]<sub>3</sub><sup>−</sup>, inducing a phase transition accompanied by a step-like change in the dielectric physical properties.

**Keywords:** phase transition; switchable dielectricity; organic–inorganic hybrid; crystal materials; three-dimensional structure



**Citation:** Hu, H.-Z.; Yan, Y.-B.; Wang, N.; Adila, A.; Liu, Y.; Liu, Z.-Q. Phase Transition and Switchable Dielectric Properties of a Three-Dimensional Hydrogen-Bonding Framework Based on Cobalt (III), *o*-Bromoaniline, and 18-Crown-6. *Crystals* **2024**, *14*, 87. <https://doi.org/10.3390/cryst14010087>

Academic Editor: Maxim V. Gorkunov

Received: 15 December 2023

Revised: 11 January 2024

Accepted: 11 January 2024

Published: 16 January 2024



**Copyright:** © 2024 by the authors. Licensee MDPI, Basel, Switzerland. This article is an open access article distributed under the terms and conditions of the Creative Commons Attribution (CC BY) license (<https://creativecommons.org/licenses/by/4.0/>).

## 1. Introduction

Molecular machines have attracted significant interest in the field of materials science owing to their wide application in sensors, gas storage, smart materials, and high-energy materials [1–4]. These molecular devices aim to convert energy into controllable movements in response to variations in temperature, pressure, light, electric or magnetic fields, and other external stimuli [5–10]. Among the family of molecular machines, solid molecular rotors, as components of artificial molecular machinery, have received much attention for their dynamic and physical properties [11–14].

Recent studies have reported the design of solid materials endowed with remarkable dynamics in their various components [15–18]. A class of materials that exhibit open-framework structures is the category of organic–inorganic hybrid supermolecular materials. These hybrids stand out for their diverse range of attributes compared to specific pure organic supermolecular compounds, such as optical, magnetic, ferroelectric, and dielectric properties while allowing easy structural tunability, excellent processability, non-toxicity, lightweight qualities, flexibility, and the occurrence of well-defined symmetry-breaking phase transitions [19–23].

Typically, electrical, magnetic, or optical responses tend to change abruptly close to the phase transition temperature. Organic–inorganic hybrids have emerged as favorable candidates for integrating phase transition properties with diverse switching response characteristics [24–28]. For responsive dielectrics, the dipolar orientation (e.g., order–disorder or melting/frozen-like transition) is the primary contributor to the dielectric constant. For

example, polar molecules or functional groups often yield switchable dielectric constants, undergoing dielectric transitions between high and low dielectric states [29–36].

Xiong et al., presented a new organic–inorganic hybrid molecular ferroelectric, [cyclopentylammonium]<sub>2</sub>CdBr<sub>4</sub>(1), showing a moderate above-room-temperature  $T_C$  of 340.3 K. The mechanism of the ferroelectric phase transition from Pnam to Pna2<sub>1</sub> in **1** is ascribed to the order–disorder transition of both the organic cations and inorganic anions [37,38]. Cyanogen metal complexes have a relatively stable thermal energy structure. If it is introduced into the molecular motor system, it will effectively improve the thermal stability of inorganic–organic hybrid functional materials [39–43]. One example is (DMA)<sub>2</sub>(H<sub>2</sub>O)[Co(CN)<sub>6</sub>] (DMA = dimethylammonium cation), with two-dimensional frameworks of the (H<sub>2</sub>O)[Co(CN)<sub>6</sub>] and (DMA)[Co(CN)<sub>6</sub>] components arranged alternately through hydrogen bonding [41]. The compound demonstrates how intermolecular interactions control crystal packing and influence the dynamics of the polar components, which are responsible for the switchable dielectric properties.

To design an organic–inorganic hybrid supermolecular rotor, it is necessary to select appropriate organic and inorganic components. Macrocyclic ligands such as crown ethers have been the subject of intense research for several decades owing to their superior selectivity in complexation with organic cations and metal ions [44–46]. Crown ether complexes can form non-covalent and hydrogen-bonded complexes with ammonium cations in both solution and solid states [47–49]. Typically, 18-crown-6 and its derivatives display the strongest affinities for organic ammonium cations (NH<sub>4</sub><sup>+</sup>, RNH<sub>3</sub><sup>+</sup>, R<sub>2</sub>NH<sub>2</sub><sup>+</sup>, etc.) in a 1:1 stoichiometry, as observed in numerous studies. However, certain structurally characterized complexes of crown ethers with RNH<sub>3</sub><sup>+</sup> exhibit varying stoichiometries, as highlighted in specific studies [50,51].

In our previous work, we discovered that the protonated organic amine RNH<sub>3</sub><sup>+</sup> cation (R = organic group) can be easily anchored within the cavity of 18-crown-6 and act as a rotator or pendulator in the design of molecular machines. Such interactions can create effective structural polarizations, providing a novel way to reveal the structure–property relationship [52,53]. By using this method, several new crown ether clathrates, such as 3-methoxyanilinium-18-crown-6 bis(trifluoromethanesulfonyl)ammonium ([3-methoxyanilinium)(18-crown-6)][trifluorosulfuric acid] [54] and [15-crown-5][Y(NO<sub>3</sub>)<sub>2</sub>(H<sub>2</sub>O)<sub>5</sub>][NO<sub>3</sub>] [55] were synthesized with large dielectric anomalies at 260 K. These studies clearly show that different organic amines and anions have significant impacts on the phase transition temperatures and polarization intensity.

Building upon the insights from previous discoveries, we synthesized a new hybrid compound, (*o*-BrAH)[H<sub>2</sub>Co(CN)<sub>6</sub>]<sub>0.5</sub>·(18-crown-6)<sub>0.5</sub>·H<sub>2</sub>O (*o*-BrAH = *o*-bromoaniline), denoted as compound **1**, exhibiting intricate cage-like hydrogen-bonded three-dimensional frameworks. Subsequently, the phase transition and switchable dielectric constant of **1** were verified using scanning calorimetry, single-crystal X-ray diffraction, and variable-temperature dielectric constant measurements. Our results showed that the dielectric transition of **1** originated mainly from the stretching deformation of the space between the cobalt atoms of the vertex of the cage-like structures.

## 2. Materials and Methods

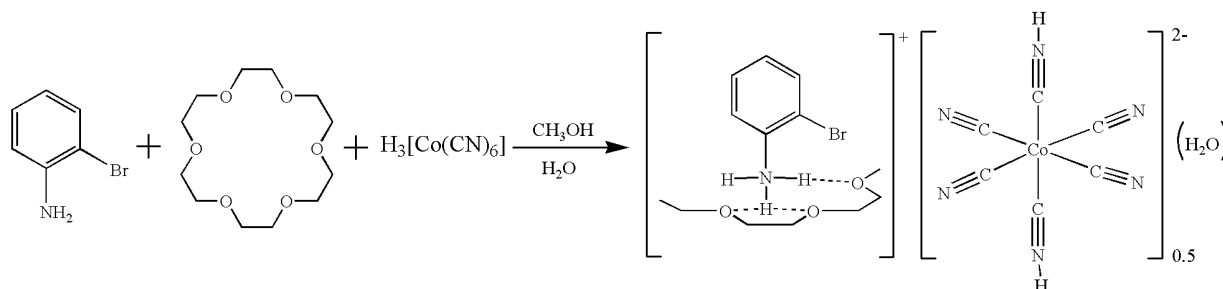
### 2.1. Material and Instruments

All chemicals and solvents purchased from commercial sources were of analytical grade and were used directly without any further purification. Elemental (C, H, and N) analyses were performed using a Varo EL Elementar Analysen System GmbH (Hanau, Germany). Thermogravimetric (TG) and differential thermal analysis (DTA) were carried out by TA Q50 thermal analyzer (New Castle, DE, USA) in the temperature range of 300–860 K under a nitrogen atmosphere at a heating rate of 10 K min<sup>−1</sup>. Differential scanning calorimetry (DSC) measurements were carried out on a TA Q2000 (TA Instruments Inc., New Castle, DE, USA) for a single-crystal sample between 200 and 350 K at a temperature scanning rate of 10 K min<sup>−1</sup>. The excess heat capacity associated with the phase transition was evaluated

by subtracting from the data the baseline representing the variation in the absence of the phase transitions. Infrared spectra (IR) were recorded on a Thermo Scientific Nicolet iS5 (Waltham, MA, USA) instrument at room temperature, within the range of 400–4000  $\text{cm}^{-1}$ . Powder X-ray diffraction (PXRD) data were collected on a BrukerD2 PHASER powder diffractometer operating at 40 kV and 30 mA using Cu  $K\alpha$  radiation with  $\lambda = 1.5418 \text{ \AA}$  for  $2\theta$  of 5 to  $50^\circ$ . The crystal and copper wire were stuck together with silver glue to form the corresponding capacitor structure. The dielectric permittivity was measured using a TH2828A precision LCR meter in the temperature range of 150–295 K at frequencies ranging from 500 Hz to 1 MHz. The commonly used equipment for testing dielectric constant is the TH2828A precision LCR instrument. Select a single crystal with complete structure, apply uniform silver glue on both sides of the single crystal, and then connect the copper wire with the silver glue. The other end of the copper wire is connected to both sides of the small circuit board to form a capacitor structure, and then, connect the small circuit board to the dielectric device. In the range of temperature 150–295K at frequencies ranging from 500 Hz to 1 MHz, a better curve of dielectric constant change is obtained through the gradual change of temperature and frequency.

## 2.2. Preparation of $(o\text{-BrAH})[\text{H}_2\text{Co}(\text{CN})_6]_{0.5}\cdot(18\text{-Crown-6})_{0.5}\cdot\text{H}_2\text{O}$ (**1**)

Compound **1** was obtained by slow evaporation of methanol solution. As shown in Scheme 1, three clean beakers were prepared and 10 mL of methanol was added, and 0.76 mmol (130.73 mg) *o*-bromoaniline, 0.76 mmol (200.00 mg) 18-crown-6, and 0.76 mmol (166.13 mg) cobalt cyanide  $\text{H}_3[\text{Co}(\text{CN})_6]$  were added, respectively. First, *o*-bromoaniline was fully mixed with 18-crown-6 methanol solution. Then, the methanol solution of cobalt cyanide  $\text{H}_3[\text{Co}(\text{CN})_6]$  was carefully added in a dropwise manner to make the mixed solution fully mixed. The mixed solution (30 mL) was evaporated at room temperature for one week to obtain yellow crystals. The yield of the product is about 67%.



**Scheme 1.** Synthesis of compound **1**.

The analytical calculated composition for  $\text{C}_{15}\text{H}_{22}\text{BrN}_4\text{O}_4\text{Co}_{0.5}$  was as follows: C, 41.73%; H, 5.14%; N, 12.98%. The actual found composition was C, 41.51%; H, 5.31%; N, 12.76%.

## 2.3. Crystal Structure Determination

Single-crystal X-ray diffraction experiments at 100 K and 296 K were conducted using a Bruker Smart ApexII single-crystal diffractometer with Mo  $K\alpha$  radiation ( $\lambda = 0.71073 \text{ \AA}$ ). Data reduction and absorption correction were carried out using SAINT and SADABS software packages, respectively. The crystal structures at different temperatures were resolved via direct methods using the SHELXL-97 software package. Non-H atoms were refined anisotropically, and all H atoms were generated geometrically and refined by using a “riding” model with  $U_{\text{iso}} = 1.2 U_{\text{eq}}(\text{c})$ . Details of data collection, structure refinement, and crystallography are summarized in Table 1.

**Table 1.** Crystallographic data for compound 1.

Temperature	100 K	296 K
Chemical formula	C <sub>15</sub> H <sub>22</sub> BrN <sub>4</sub> O <sub>4</sub> Co <sub>0.5</sub>	C <sub>15</sub> H <sub>22</sub> BrN <sub>4</sub> O <sub>4</sub> Co <sub>0.5</sub>
Formula weight	431.73	431.73
Crystal size (mm <sup>3</sup> )	0.22 × 0.20 × 0.18	0.22 × 0.20 × 0.18
Crystal system	Triclinic	Triclinic
Space group	<i>P</i> -1	<i>P</i> -1
<i>a</i> (Å)	8.566(3)	8.724(3)
<i>b</i> (Å)	9.831(4)	9.687(3)
<i>c</i> (Å)	11.508(4)	11.556(4)
$\alpha$ (°)	75.764(4)	77.799(4)
$\beta$ (°)	79.755(4)	78.954(4)
$\gamma$ (°)	88.092(4)	88.451(4)
<i>V</i> (Å <sup>3</sup> )	924.3(6)	936.8(5)
<i>Z</i>	1	1
<i>D</i> <sub>calc</sub> (g cm <sup>-3</sup> )	1.549	1.529
<i>F</i> (000)	440	440
$\mu$ (mm <sup>-1</sup> )	2.683	2.647
Measured 2 $\theta$ range (°)	0.980–25.242	0.898–25.242
<i>R</i> <sub>int</sub>	0.0489	0.0700
<i>R</i> ( <i>I</i> > 2( <i>I</i> )) [ <i>a</i> ]	0.0579	0.0947
<i>wR</i> (all data) [ <i>b</i> ]	0.1343	0.1918
GOF	1.088	1.054
CCDC	2313124	2313125

$$[a] : R = \sum (|F_o| - |F_c|) / \sum |F_o|$$

$$[b] : R_w^2 = \sum_w (F_o^2 - F_c^2)^2 / \sum_w (F_o^2)^2$$

### 3. Results and Discussion

#### 3.1. Spectral Properties

Each component showed the characteristic IR stretches of the individual component of the molecule (Figure S1). The IR spectra of **1** contained the characteristic peaks of 18-crown-6 molecules at 835, 955, and 1089 cm<sup>-1</sup>, corresponding to the specific –O–C–C– structural unit. The strong broad band from 3541 cm<sup>-1</sup> to 2643 cm<sup>-1</sup> indicated the intermolecular N–H···O hydrogen bonding interactions between the N atom of the protonated –NH<sub>2</sub> group and the O atoms of 18-crown-6. The series of characteristic peaks at 1599, 1563, 1348, 1300, and 1250 cm<sup>-1</sup> were assigned to the skeletal vibrations of the aromatic rings. The sharp peaks within the 2175–2050 cm<sup>-1</sup> range were characteristic of the stretching vibrations of the –C≡N bond of the [Co(CN)<sub>6</sub>]<sub>3</sub><sup>-</sup> anion. Overall, the IR spectra analysis revealed the successful incorporation of the three effective constituents (18-crown-6, *o*-bromoanilinium, and [Co(CN)<sub>6</sub>]<sub>3</sub><sup>-</sup> anion) in compound **1**.

#### 3.2. TG and DSC Analysis

In order to explore potential crystal phase transitions within compound **1** triggered by external temperature variations, we conducted sequential heating and cooling cycles between 200 and 290 K. As shown in Figure 1, an endothermic peak occurred during the heating process at a temperature of approximately 265 K, attributed to *T*<sub>c</sub>. The phases below and above *T*<sub>c</sub> were labeled as LTP (low-temperature phase) and RTP (room-temperature phase), respectively, for ease of reference.

During the cooling process, the corresponding exothermic peak shifted to a lower temperature of about 255 K. The appearance of a well-defined reversible anomaly and a large thermal hysteresis (10 K) suggested that the transition was first order. The transition enthalpy ( $\Delta H$ ) of the endothermic process was estimated to be 1.63 kJ mol<sup>-1</sup>, corresponding to an entropy change ( $\Delta S$ ) of 6.17 J mol<sup>-1</sup> K<sup>-1</sup>. The calculation of the ratio of geometrically distinguishable orientations, represented as *N*, was performed using the Boltzmann equation ( $\Delta S = R \ln N$ ), with *R* denoting the gas constant. The resulting value for *N* was

2.1, surpassing two, indicating an order–disorder mechanism rather than a displacive mechanism [56].

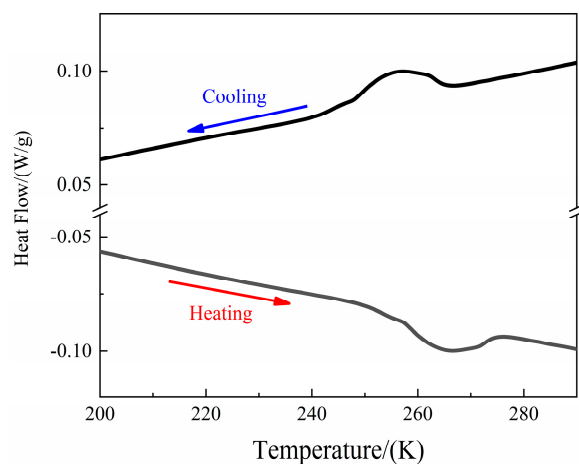


**Figure 1.** DSC curves for compound **1** during the heating process.

Thermogravimetric (TG) and differential thermal analyses (DTA) were performed in an N<sub>2</sub> atmosphere from 300 to 860 K at a heating rate of 10 K min<sup>−1</sup>. The DTA curve showed a weak endothermic peak at 382 K (Figure S2), which corresponded to the melting point of **1**. The TG curve revealed three primary weight-loss regions. Compound **1** maintained an ordered structure up to 382 K. Within the range of 382 to 429 K, the TG of compound **1** indicated an initial weight loss of 4.31% (calculated at 4.17%), attributed to the loss of a single free water molecule. The second sharp weight loss of nearly 70.31% was observed within the range of 429–519 K, where the decomposition of the supramolecular cation (*o*-BrAH)(18-crown-6)<sub>0.5</sub> occurred. The third weight-loss step of 25.38% (calculated at 25.14%) involved the [H<sub>2</sub>Co(CN)<sub>6</sub>]<sub>0.5</sub> anion. Overall, the DSC and TG analyses demonstrated the relatively good thermal stability of **1**.

### 3.3. XRD Analysis

The phase purity of compound **1** was determined using X-ray powder diffraction (XRD). Comparison between the peak positions in both the experimental and simulated XRD patterns indicated good agreement (Figure 2). This result confirmed the successful acquisition of compound **1** in a pure crystalline phase. The difference in the intensity was attributed to the preferred orientation of the powder sample.

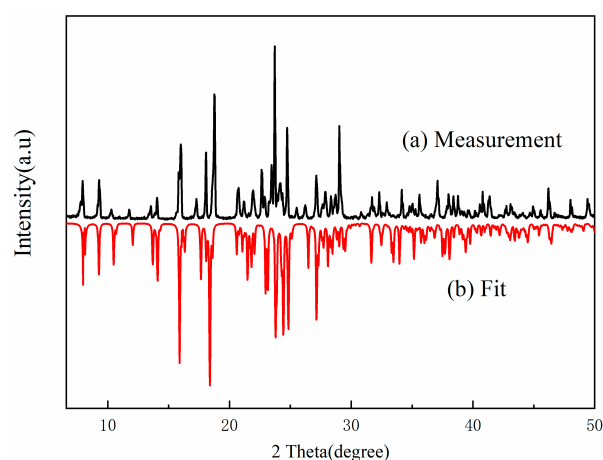


**Figure 2.** Experimental XRD pattern (a) and simulated pattern (b) of compound **1**.

### 3.4. Description of Crystal Structure

To understand the origin of the reversible phase transition of compound **1**, variable-temperature single-crystal X-ray structural analyses were performed at 100 K (LTP) and 296 K (RTP). The  $(o\text{-BrAH})[\text{H}_2\text{Co}(\text{CN})_6]_{0.5}\cdot(18\text{-crown-6})_{0.5}\cdot\text{H}_2\text{O}(1)$  structure crystallized in a centrosymmetric triclinic crystal system with space group  $P\bar{1}$  (No. 2) at both LTP and RTP, indicating the existence of reversible iso-symmetric structural phase transitions. The complete crystallographic data and their collection and refinement are presented in Table 1.

Considering the minor alterations in cell parameters observed between LTP and RTP, it implies that factors beyond the phase transition, such as the presence of a distorted octahedral cation or molecular frame motion, could be contributing to this phenomenon.

The asymmetric units of the LTP and RTP of compound **1** comprised one  $o\text{-BrAH}$  cation, one-half of the 18-crown-6 molecule, and one-half of the  $[\text{H}_2\text{Co}(\text{CN})_6]$  anion (Figure 3a,b). Figure 3 shows that the atomic temperature factor increased, indicating heightened thermal vibrations across all atoms as the temperature was increased from LTP to RTP. In addition, the thermal ellipsoids of the C, N, and O atoms of the 18-crown-6 molecule and  $o\text{-BrAH}$  cations showed significant changes from LTP to RTP. Such thermal ellipsoid changes can be attributed to the intermolecular oscillation or motion of the supramolecular cation  $(o\text{-BrAH})(18\text{-crown-6})$  upon heating, leading to detectable heat changes in compound **1**.

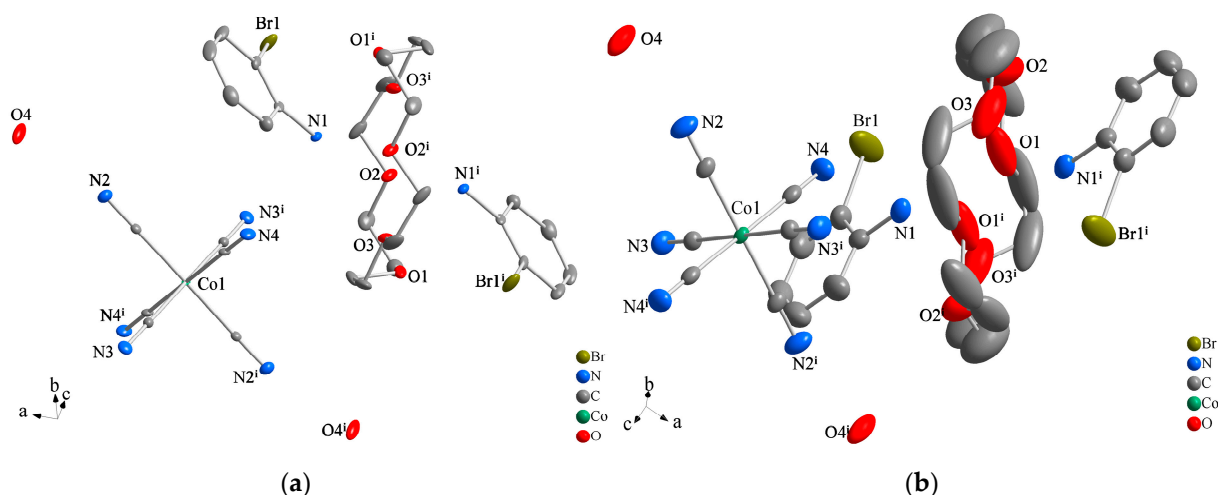


**Figure 3.** Molecular structure of compound **1** at different temperatures: (a) asymmetric unit at 100 K, (b) asymmetric unit at 296 K.

In Figure 4, the cell of compound **1** contains two  $[\text{H}_2\text{Co}(\text{CN})_6]$  anions and two supramolecular cations  $(o\text{-BrAH})(18\text{-crown-6})$ . During the process from low temperature to room temperature, the distance between the two cobalt atoms and the planes of the two crown ethers increases from 11.508 Å to 11.556 Å and 8.138 Å to 8.288 Å, respectively. This is mainly due to the thermal expansion of molecules.

The change in supramolecular cations between the two phases is crucial for determining the origin of the structural phase transition. The most striking structural feature in the LTP and RTP is the tripolymer supramolecular cation structure  $(o\text{-BrAH})_2(18\text{-crown-6})$  with two  $o\text{-BrAH}$  cations and one 18-crown-6 molecule connected through  $\text{N}\cdots\text{H}\cdots\text{O}$  hydrogen-bonding interactions. The oxygen atoms of 18-crown-6 are displaced above ( $\text{O}_1, \text{O}_2, \text{O}_3$ ) and below ( $\text{O}_1^i, \text{O}_2^i, \text{O}_3^i$ ) the median plane of the ring, resulting in two completely parallel triangular planes.

The N atom of the  $o\text{-BrAH}$  cation is positioned in the perching configuration rather than the nesting configuration, resting at distances of 1.309 Å (LTP) and 1.422 Å (RTP) above the optimal plane formed by the O atoms of the 18-crown-6. Six hydrogen bondings exist between the O atoms of 18-crown-6 and the N atoms of the  $o\text{-BrAH}$  cation, where the short distance of  $\text{N}\cdots\text{H}\cdots\text{O}$  signifies strong interactions in the range of 2.832–3.188 Å at 100 K, and 2.844–3.220 Å at 296 K. In addition, the aromatic ring of the  $o\text{-BrAH}$  cation forms

smaller dihedral angles to the O atom plane of the 18-crown-6 molecule, measuring  $38.14^\circ$  (LTP) and  $40.83^\circ$  (RTP) (Figure S3). This dihedral angle underwent a significant change with the temperature increase, suggesting that the angular change in the intermolecular oscillation of the supramolecular cation can affect the structural phase transition of **1**.

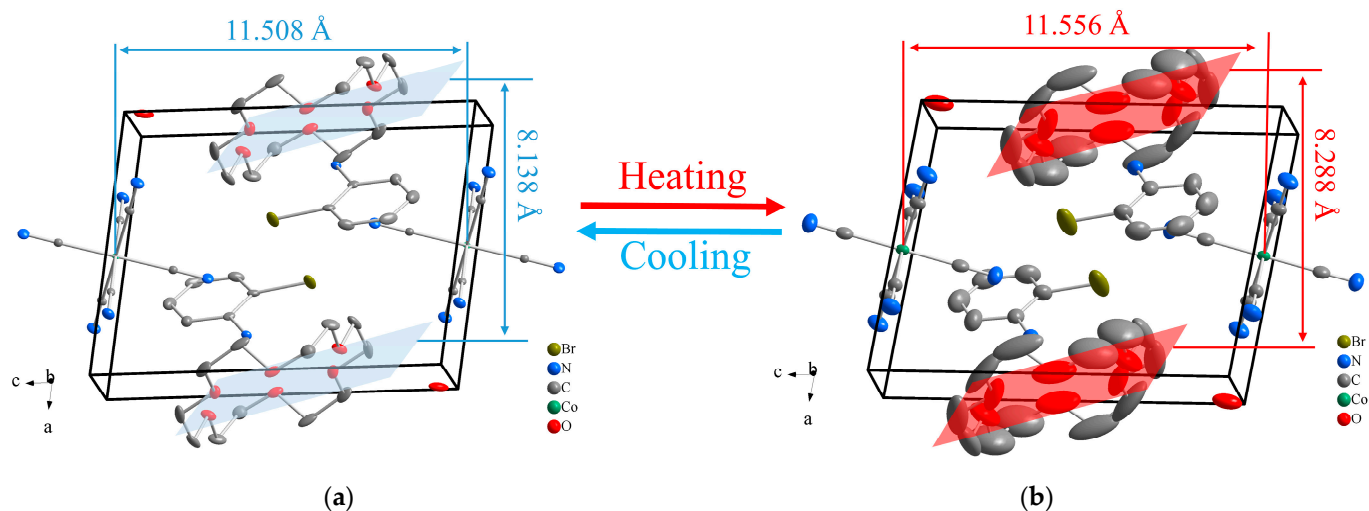


**Figure 4.** The change of the cell at different temperatures: (a) at 100 K (b) at 296 K.

To determine the coordination configuration of the Co ions, we analyzed the structures of the metal complexes at different temperatures. The Co–C bond lengths were in the range of 1.902–1.909 Å (LTP) and 1.901–1.911 Å (RTP), and the Co–C–N angles were from  $178.84$  to  $179.64^\circ$  (LTP) and  $178.18$  to  $179.45^\circ$  (RTP), generally close to  $180^\circ$ . Through all its six  $\text{CN}^-$  groups, two CN groups connected to two protons to form the new coordinating C–N–H<sup>+</sup> group.

Because of the hydrogen protons, each water molecule formed three different types of hydrogen bonds: O–H $\cdots$ O, O–H $\cdots$ N, and N–H $\cdots$ O, forming connections with surrounding water molecules and two  $[\text{H}_2\text{Co}(\text{CN})_6]$  anions (Figure 5a). The hydrogen bond lengths were 2.489 Å (LTP) and 2.479 Å (RTP) for O–H $\cdots$ O, 2.744 Å (LTP) and 2.715 Å (RTP) for O–H $\cdots$ N, and 2.704 Å (LTP) and 2.732 Å (RTP) for N–H $\cdots$ O (Table S1). This result indicated that, compared to the alterations in the Co–C bonds of the  $[\text{H}_2\text{Co}(\text{CN})_6]$  anion, the hydrogen bond lengths underwent notable changes with the temperature increase.

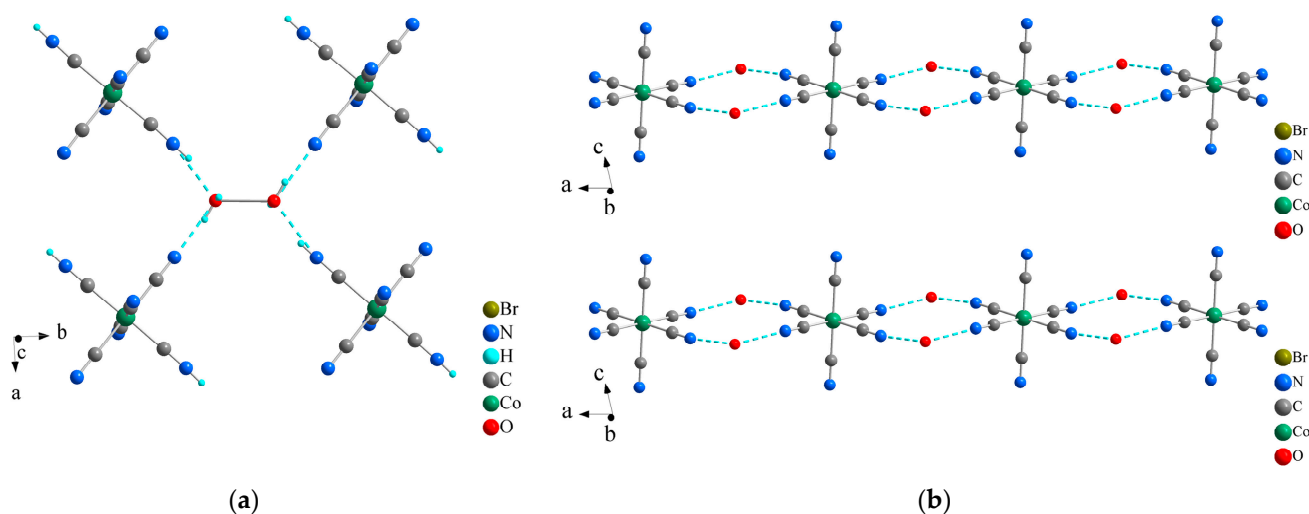


**Figure 5.** (a) Molecular structure of water and cobalt cyanide anions; (b) N–H $\cdots$ O hydrogen bonds formed between cobalt cyanide anions and O atoms in adjacent water molecules.

The two  $[\text{H}_2\text{Co}(\text{CN})_6]$  anions established connections with two adjacent water molecules through the interaction of  $\text{N}-\text{H}\cdots\text{O}$  and  $\text{O}-\text{H}\cdots\text{N}$  hydrogen bonds, forming a one-dimensional chain structure that extended along the  $a$ -axis direction (Figure 5b). The Co–Co distances, bridged by the  $\text{CN}^-$  groups and water molecules in adjacent  $[\text{H}_2\text{Co}(\text{CN})_6]$  anions, ranged from 8.566 Å (LTP) to 8.724 Å (RTP) with the temperature changes. These changes in the hydrogen bond lengths and Co–Co distances clearly indicated that the molecular interaction was related to the phase transition and the corresponding changes in physical properties.

The two water molecules in the one-dimensional chain structure were connected to each other through  $\text{O}-\text{H}\cdots\text{O}$  hydrogen bonds, creating a two-dimensional layered structure in the  $ab$  plane (Figure 6a), providing sufficient space for the  $(o\text{-BrAH})_2(18\text{-crown-6})$  cation interpenetration. The interlayer distances between the averaged planes were 11.508 Å at LTP (Figure 6b) and 11.556 Å at RTP, indicating a significant distance elongation with increasing temperature.

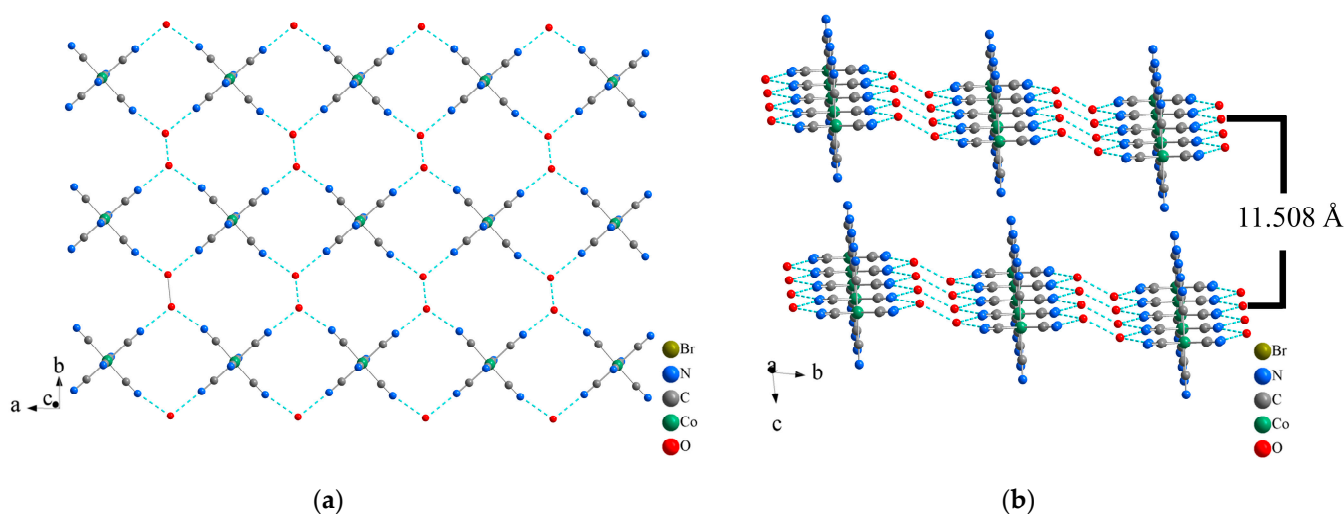


**Figure 6.** (a) Two-dimensional layered structure of compound **1**. (b) Distance between cobalt atoms in adjacent layers.

The two protonated 2-bromoanilines in the dimer structure interacted with the crown ether molecules through  $\text{N}-\text{H}\cdots\text{O}$  hydrogen bonds (Figure 7c). Complex **1** exhibited a three-dimensional supermolecular architecture, which can be visualized as connected dimer and 2D layer structures in the  $ab$  plane through  $\text{N}-\text{H}\cdots\text{N}$  hydrogen-bond interactions between the remaining  $-\text{C}\equiv\text{N}$  ligand of the  $[\text{H}_2\text{Co}(\text{CN})_6]$  anion and the  $-\text{NH}_3^+$  group of the  $(o\text{-BrAH})_2(18\text{-crown-6})$  cation (Figures 7a and S4). A new type of framework was formed inside the crystal, in which the Co atoms were positioned in its vertices, presenting a hexahedral cage-like structure (Figure 7b). Notably, the supramolecular cation  $(o\text{-BrAH})_2(18\text{-crown-6})$  occupied the space within the hexahedral cage-like structure, resulting in the formation of a novel filling arrangement (Figures 7d and S5).

The most notable feature of the three-dimensional cage-like structure was the parallelepiped structure consisting of the eight cobalt (III) ions from the  $[\text{H}_2\text{Co}(\text{CN})_6]$  anions (Figure 8). In LTP, the non-bonding angle values of the central  $\text{Co}\cdots\text{Co}\cdots\text{Co}$  atoms were  $97.871^\circ$ ,  $118.856^\circ$ , and  $100.254^\circ$ , respectively. However, in the RTP, the non-bonding angle in the same position as the parallelepiped exhibited a notable change at temperature increments of  $84.009^\circ$ ,  $91.674^\circ$ , and  $106.350^\circ$ .

By comparing the distances of adjacent  $\text{Co}\cdots\text{Co}$  atoms in the two LTP and RTP structures, the adjacent  $\text{Co}\cdots\text{Co}$  distances of 12.823 Å and 13.253 Å along the  $b$ - and  $a$ -axis orientation in the LTP structure resembled those of 12.860 Å and 13.210 Å for the RTP structure. In contrast, the adjacent  $\text{Co}\cdots\text{Co}$  distance of 13.067 Å along the  $c$ -axis orientation in the LTP structure was determined to be longer than that in the RTP structure (11.556 Å), representing a significant change of 11.56%. These results suggested that the transforma-

tion of the parallelepiped structure along the  $c$ -axis through temperature changes caused structural phase transitions and dielectric anomalies.

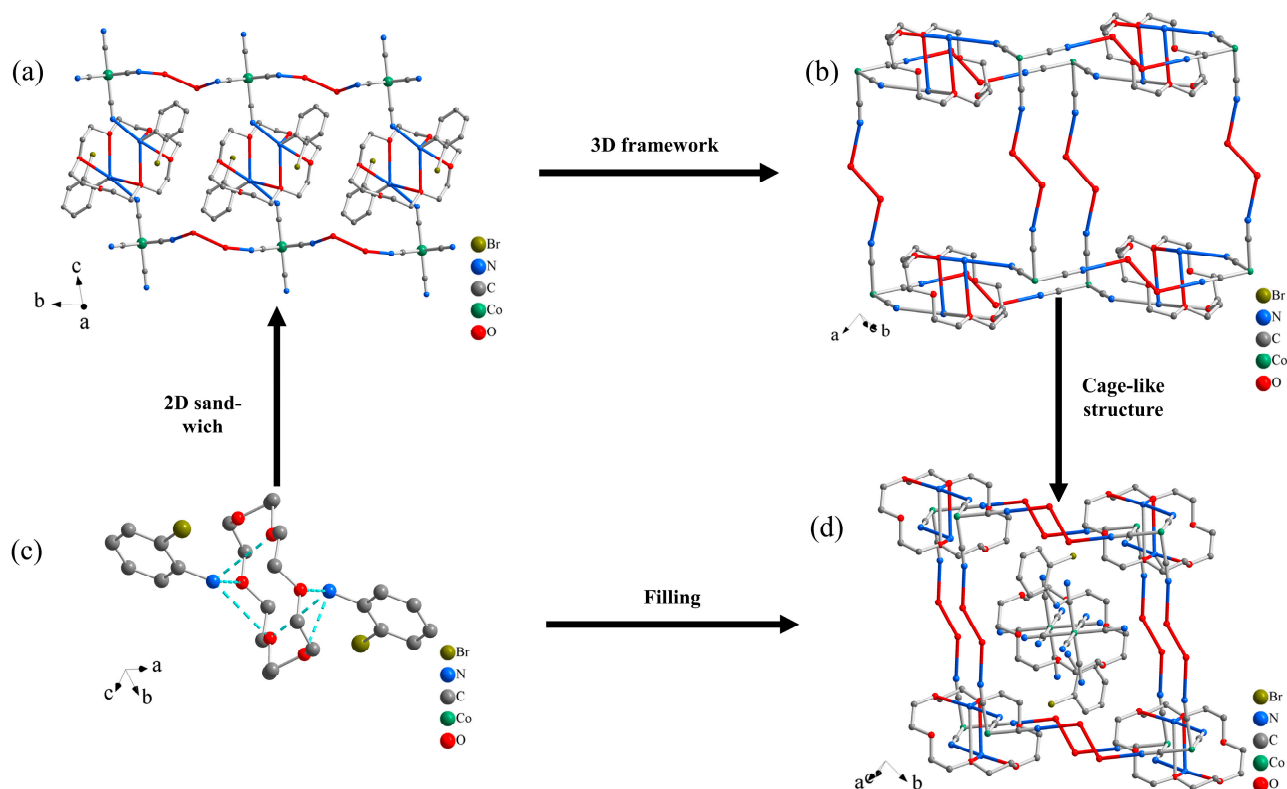


**Figure 7.** (a) Two-dimensional layered structure formed by (18-crown-6)(*o*-BrAH) and [Co(CN)<sub>6</sub>] through hydrogen bonds. (b) Three-dimensional cage-like construction formed by 2D layered structure and two water molecules. (c) Dimeric structure of (18-crown-6)(*o*-BrAH)<sub>2</sub>. (d) Cage-like clathrate hydrate structure filled with the dimer.

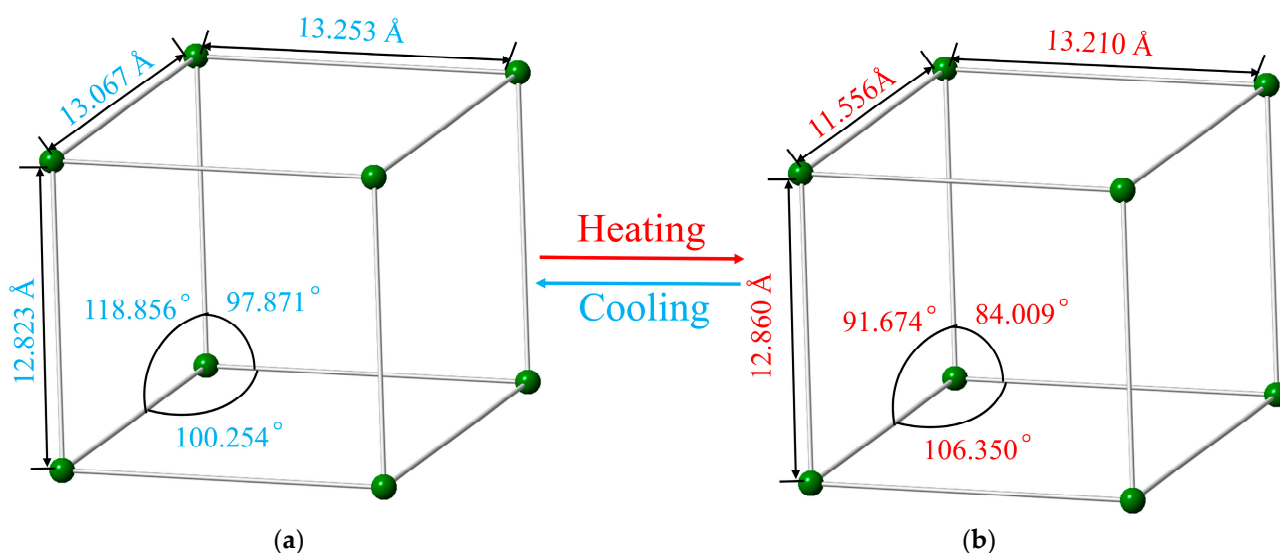


**Figure 8.** Three-dimensional cage-like construction at (a) 100 K and (b) 296 K.

### 3.5. Dielectric Properties

Various physical property anomalies change sharply near the phase transition temperature, and the degree of change is related to the characteristics of the phase transitions. The temperature- and frequency-dependent dielectric constants are effective indicators of

the structural phase transitions. In the mechanism of the phase transition confirmed by DSC and the low- and room-temperature X-ray results mentioned above, compound **1** was presumed to exhibit a dielectric anomaly response triggered by changes in the temperature and electric field frequency.

Dielectric measurements were performed along each axis of compound **1** after pasting the crystal with elargol-conducting glue, over the frequency range of 500 Hz to 1 MHz upon cooling and within the temperature range of 150 K to 295 K. Figure 9 shows the changes in the real part of the temperature-dependent dielectric constant upon cooling. As the temperature decreased, distinct anomalies emerged around 265 K, aligning with the findings from the DSC results.

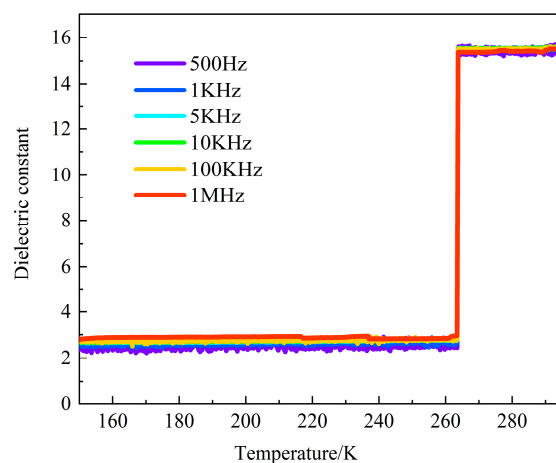


**Figure 9.** Anisotropic dielectric constants of **1** along the *c*-axis at 500 Hz to 1 MHz upon cooling.

The real part of the dielectric constant showed strong temperature dependency under an applied electric field. Throughout the cooling process, the real parts of compound **1**'s dielectric constant stayed steady at around 2.5. Between 150 K and 260 K at LTP, it exhibited a substantial increase up to approximately 16 near 265 K across all frequencies. It maintained this level until experiencing a notable temperature escalation to 295 K.

The results indicated that the dielectric constants could switch between high and low states, exhibiting two-phase transitions. These transitions allowed for tuning between two different states during the cooling processes. Furthermore, the independence of the dielectric constant from the frequency in the temperature range of 150–295 K indicated the absence of molecular motor rotation in the crystal.

Such temperature-triggered switching dielectric behavior is related to the intermolecular oscillation of the supramolecular cation (*o*-BrAH)(18-crown-6). At higher temperatures, the thermal vibrations of the atoms are intensified. The adjacent Co–Co distances of the parallelepiped in the crystal space varied between RTP and LTP, indicating notable deformation of the parallelepiped. As a result, the thermally activated intermolecular oscillation of the supramolecular cation and the deformation of the parallelepiped lead to dielectric anomalies.

#### 4. Conclusions

In summary, we present a novel organic–inorganic hybrid compound, (*o*-BrAH)[H<sub>2</sub>Co(CN)<sub>6</sub>]<sub>0.5</sub>·(18-crown-6)<sub>0.5</sub>·H<sub>2</sub>O (**1**), with a three-dimensional hydrogen-bonding cage-like structure. The integration of low- and room-temperature structural analyses, DSC measurements, and dielectric measurements successfully showcased compound **1** as a new switchable molecular dielectric material. This material exhibits reversible structural phase transitions at 265 K and can be tuned to two distinct dielectric states by varying the temperature. Different temperature structure analyses revealed that the structural phase transition and dielectric anomaly were related to the intermolecular oscillation of the supramolecular cation and deformation of the parallelepiped structure at the eight cobalt (III) centers in

the  $[\text{H}_2\text{Co}(\text{CN})_6]$  anion. The switchable nature of the dielectric constant in **1** enhances the diversity of responsive dielectric materials within its family.

**Supplementary Materials:** The following supporting information can be downloaded at <https://www.mdpi.com/article/10.3390/cryst14010087/s1>, Figure S1: IR spectrum of compound **1**; Figure S2: TG and DTA curves of compound **1**; Table S1: Hydrogen bond N–H...O geometry (Å, °) for compound **1**; Figure S3: Swing diagram of crown ether cation complex *o*-BrAH of compound **1** at room and low temperature; Figure S4: *ac* planar graph of compound **1**; Figure S5: *bc* planar graph of compound **1**.

**Author Contributions:** Conceptualization, Z.-Q.L. and Y.L.; methodology, H.-Z.H.; software, N.W.; validation, H.-Z.H.; formal analysis, Y.-B.Y.; investigation, H.-Z.H. and A.A.; resources, Z.-Q.L.; data curation, H.-Z.H.; writing—original draft preparation, Y.L.; writing—review and editing, Z.-Q.L.; project administration, Z.-Q.L.; funding acquisition, Z.-Q.L. All authors have read and agreed to the published version of the manuscript.

**Funding:** This research was funded by the General Program of Natural Science Foundation of Xinjiang Uygur Autonomous Region (Grant No.2022D02A76); Key Research and Development Projects of the Xinjiang Uygur Autonomous Region (Grant No. 20220264-3); the Key R&D Plan Project in Xinjiang Autonomous Region (2022B02033-3, 2022B02049-3); the National Natural Science Foundation of China (Grant No. 21561030); the Xinjiang “Tianshan talent plan” project (Grant No. 2021061); and the Open Research Fund of Xinjiang Key Laboratory of Agricultural Chemistry and Biomaterials (KF202206).

**Data Availability Statement:** Data are contained within the article and Supplementary Materials.

**Conflicts of Interest:** The authors declare no conflicts of interest. The funders had no role in the design of study; in the collection, analyses, or interpretation of data; in the writing of the manuscript; or in the decision to publish the results.

## References

1. Hua, X.-N.; Huang, C.-R.; Gao, J.-X.; Lu, Y.; Chen, X.-G.; Liao, W.-Q. High-temperature Reversible Phase Transitions and Exceptional Dielectric Anomalies in Cobalt (II) Based Ionic Crystals:  $[\text{Me}_3\text{NCH}_2\text{X}]_2[\text{CoX}_4]$  (X = Cl and Br). *Dalton Trans.* **2018**, *47*, 6218–6224. [[CrossRef](#)]
2. Lai, H.J.; He, F. Crystal Engineering in Organic Photovoltaic Acceptors: A 3D Network Approach. *Adv. Energy Mater.* **2020**, *10*, 2002678. [[CrossRef](#)]
3. Li, D.; Zhao, X.M.; Zhao, H.X.; Long, L.S.; Zheng, L.S. Coexistence of Magnetic-Optic-Electric Triple Switching and Thermal Energy Storage in a Multifunctional Plastic Crystal of Trimethylchloromethyl Ammonium Tetrachloroferrate(III). *Inorg. Chem.* **2019**, *58*, 655–662. [[CrossRef](#)]
4. Xu, C.; Zhang, W.-Y.; Ye, Q.; Fu, D.-W. Multifunctional Material with Efficient Optoelectronic Integrated Molecular Switches Based on a Flexible Thin Film/Crystal. *Inorg. Chem.* **2017**, *56*, 14477–14485. [[CrossRef](#)] [[PubMed](#)]
5. Tao, K.; Han, S.; Ji, C.; Liu, X.; Wu, Z.; Zhang, J.; Luo, J.; Sun, Z. Structural Phase Transition and Switchable Dielectric Properties of a Unique Two-Dimensional Organic–Inorganic Hybrid Perovskite Compound  $[\text{C}_6\text{H}_{11}\text{NH}_2\text{CH}_3]_4\text{Pb}_3\text{I}_{10}$ . *Cryst. Growth Des.* **2018**, *18*, 7316–7322. [[CrossRef](#)]
6. García-Fernández, A.; Bermúdez-García, J.M.; Castro-García, S.; Llamas-Saiz, A.L.; Artiaga, R.; López-Beceiro, J.; Hu, S.; Ren, W.; Stroppa, A.; Sánchez-Andújar, M.; et al. Phase Transition, Dielectric Properties, and Ionic Transport in the  $[(\text{CH}_3)_2\text{NH}_2]\text{Pb}_3$  Organic-Inorganic Hybrid with 2H-Hexagonal Perovskite Structure. *Inorg. Chem.* **2017**, *56*, 4918–4927. [[CrossRef](#)]
7. Ji, Q.; Li, L.; Deng, S.; Cao, X.; Chen, L. High Switchable Dielectric Phase Transition Originating from Distortion in Inorganic–Organic Hybrid Materials  $(\text{H}_2\text{dabco}-\text{C}_2\text{H}_5)[\text{M}^{\text{II}}\text{Cl}_4]$  (M = Co, Zn). *Dalton Trans.* **2018**, *47*, 5630–5638. [[CrossRef](#)] [[PubMed](#)]
8. He, L.; Xu, K.; Shi, P.-P.; Ye, Q.; Zhang, W. An Order–Disorder Type High-Temperature Multiaxial Supramolecular Ferroelectric. *Adv. Electron. Mater.* **2022**, *8*, 2100635. [[CrossRef](#)]
9. Drath, O.; Boskovic, C. Switchable Cobalt Coordination Polymers: Spin Crossover and Valence Tautomerism. *Coord. Chem. Rev.* **2018**, *375*, 256–266. [[CrossRef](#)]
10. Duncan, H.D.; Beake, E.O.R.; Playford, H.Y.; Dove, M.T.; Phillips, A.E. Local Structure of a Switchable Dielectric Prussian Blue Analogue. *CrystEngComm* **2017**, *19*, 7316–7321. [[CrossRef](#)]
11. Luo, H.-B.; Wang, M.; Liu, S.-X.; Liu, W.-L.; Zou, Y.; Tian, Z.-F.; Ren, S.-M. Both Dielectrics and Conductance Anomalies in an Open-Framework Cobalt Phosphate. *Inorg. Chem.* **2017**, *56*, 13998–14004. [[CrossRef](#)]
12. Jiang, F.; Wang, C.-F.; Wu, Y.-X.; Li, H.-H.; Shi, C.; Ye, H.-Y.; Zhang, Y. Nonlinear Optical and Photoluminescence Bistable Responses Accompanied by Tunable Dielectric Behaviors in Crown Inclusions. *J. Phys. Chem. C* **2020**, *124*, 5796–5801. [[CrossRef](#)]

13. Zhang, Y.; Ye, H.-Y.; Cai, H.-L.; Fu, D.-W.; Ye, Q.; Zhang, W.; Zhou, Q.-H.; Wang, J.-I.; Yuan, G.-L.; Xiong, R.-G. Switchable Dielectric, Piezoelectric, and Second-Harmonic Generation Bistability in a New Improper Ferroelectric above Room Temperature. *Adv. Mater.* **2014**, *26*, 4515–4520. [[CrossRef](#)]
14. Tang, Y.-Z.; Yu, Y.-M.; Xiong, J.-B.; Tan, Y.-H.; Wen, H.-R. Unusual High-Temperature Reversible Phase-Transition Behavior, Structures, and Dielectric–Ferroelectric Properties of Two New Crown Ether Clathrates. *J. Am. Chem. Soc.* **2015**, *137*, 13345–13351. [[CrossRef](#)]
15. Liu, X.; Xiao, Y.; Zhang, Z.; You, Z.; Li, J.; Ma, D.; Li, B. Recent Progress in Metal–Organic Frameworks@Cellulose Hybrids and Their Applications. *Chin. J. Chem.* **2021**, *39*, 3462–3480. [[CrossRef](#)]
16. Rok, M.; Prytys, J.K.; Kinzhybalov, V.; Bator, G. Flexible Crystals of Perovskite-like Coordination Polymers with a Tunable and Switchable Organic Guest:  $(\text{CH}_3\text{NH}_3)_2[\text{KFe}(\text{CN})_6]$  and  $(\text{CH}_3\text{NH}_3)_2[\text{KCo}(\text{CN})_6]$ . *Dalton Trans.* **2017**, *46*, 2322–2331. [[CrossRef](#)] [[PubMed](#)]
17. Lin, R.; Li, X.; Krajnc, A.; Li, Z.; Li, M.; Wang, W.; Zhuang, L.; Smart, S.; Zhu, Z.; Appadoo, D.; et al. Mechanochemically Synthesised Flexible Electrodes Based on Bimetallic Metal–Organic Framework Glasses for the Oxygen Evolution Reaction. *Angew. Chem. Int. Ed.* **2022**, *61*, e202112880. [[CrossRef](#)] [[PubMed](#)]
18. Ye, H.-Y.; Ge, J.-Z.; Tang, Y.-Y.; Li, P.-F.; Zhang, Y.; You, Y.-M.; Xiong, R.-G. Molecular Ferroelectric with Most Equivalent Polarization Directions Induced by the Plastic Phase Transition. *J. Am. Chem. Soc.* **2016**, *138*, 13175–13178. [[CrossRef](#)] [[PubMed](#)]
19. Szostak, E.; Pinkowicz, D.; Fryń, P.; Marzec, M. Investigation of Correlation Between Phase Transformations and Changes in Structural, Dynamic, Magnetic and Dielectric Properties of Hexakis-DMSO Cobalt (II) Complex. *J. Mol. Struct.* **2019**, *1194*, 227–235. [[CrossRef](#)]
20. Khan, S.; Alothman, Z.A.; Mohammad, M.; Islam, M.S.; Slawin, A.; Wabaidur, S.M.; Islam, M.M.; Mir, M.H. Synthesis and Characterization of a Hydrogen Bonded Metal–Organic Cocrystal: Exploration of its DNA Binding Study. *Polyhedron* **2020**, *180*, 114454. [[CrossRef](#)]
21. Nemeč, V.; Lisac, K.; Bedeković, N.; Fotović, L.; Stilinović, V.; Cinčić, D. Crystal Engineering Strategies Towards Halogen-Bonded Metal–Organic Multi-Component Solids: Salts, Cocrystals and Salt Cocrystals. *CrystEngComm* **2021**, *23*, 3063–3083. [[CrossRef](#)]
22. Rather, M.U.D.; Samad, R.; Want, B. Ferroelectric and Magneto-Dielectric Properties of Yttrium Doped  $\text{BaTiO}_3\text{-CoFe}_2\text{O}_4$  Multiferroic Composite. *J. Mater. Sci. Mater. Electron.* **2018**, *29*, 19164–19179. [[CrossRef](#)]
23. Fu, J.; Wu, Y. A Showcase of Green Chemistry: Sustainable Synthetic Approach of Zirconium-Based MOF Materials. *Chem. Eur. J.* **2021**, *27*, 9967–9987. [[CrossRef](#)] [[PubMed](#)]
24. Gong, Z.-H.; Shi, L.; Gao, X.-M.; Bi, W.-C.; Huang, X.-H.; Sun, Y.-Q.; Sun, R.-Q.; Chen, Y.-P. A Novel Photochromism Material Based on Both Pyrimidinium and Polyoxometalate:  $(\text{C}_4\text{N}_2\text{H}_4\text{-C}_4\text{N}_2\text{H}_3)[\text{Mn}(\text{H}_2\text{O})_6]_{0.5}[\text{SiW}_{12}\text{O}_{40}]_{0.5} \cdot 5\text{H}_2\text{O}$ . *J. Mol. Struct.* **2020**, *1206*, 127716. [[CrossRef](#)]
25. Liu, J.L.; Ji, X.Y.; Xue, J.P.; Hu, J.-S.; Yao, Z.-S.; Tao, J. Architectural Isomerism in the Three-Dimensional Prussian Blue Analogue  $\{[\text{Co}^{\text{II}}(\text{TPA})]_3[\text{Fe}^{\text{III}}(\text{CN})_6][\text{Co}^{\text{III}}(\text{CN})_6]\}$ : Synthesis, Crystal Structures, and Magnetic Properties. *Cryst. Growth Des.* **2022**, *22*, 5092–5099. [[CrossRef](#)]
26. Tsymbal, L.V.; Andriichuk, I.L.; Shova, S.; Lampeka, Y.D. Crystal Structure of  $\{[\text{Ni}(\text{C}_{10}\text{H}_{24}\text{N}_4)][\text{Ni}(\text{CN})_4]\} \cdot 2\text{H}_2\text{O}\}_n$ , A One-Dimensional Coordination Polymer Formed from the  $[\text{Ni}(\text{cyclam})]^{2+}$  Cation and the  $[\text{Ni}(\text{CN})_4]^{2-}$  Anion. *Acta Crystallogr. E Crystallogr. Commun.* **2021**, *77*, 1140–1143. [[CrossRef](#)] [[PubMed](#)]
27. Kuschal, C.; Botta, E.; Orioli, D.; Digiovanna, J.J.; Seneca, S.; Keymolen, K.; Tamura, D.; Heller, E.; Khan, S.G.; Caligiuri, G.; et al. GTF2E2 Mutations Destabilize the General Transcription Factor Complex TFIIE in Individuals with DNA Repair-Proficient Trichothiodystrophy. *Am. J. Hum. Genet.* **2016**, *98*, 627–642. [[CrossRef](#)]
28. Moskwa, M.; Sobieszczyk, P.; Mikurenda, J.W.; Zieliński, P.; Rok, M. Improper Ferroelastic Phase Transition in a Hydrogen-Bonded Metalloacyanide-Based (Azetidinium) $_2(\text{H}_3\text{O})[\text{Co}(\text{CN})_6]$  Framework. *Chem. Comm.* **2023**, *59*, 5535–5538. [[CrossRef](#)]
29. Stefanczyk, O.; Kumar, K.; Pai, T.; Li, G.; Ohkoshi, S.-I. Integration of Trinuclear Triangle Copper (II) Secondary Building Units in Octacyanidometallates(IV)-Based Frameworks. *Inorg. Chem.* **2022**, *61*, 8930–8939. [[CrossRef](#)]
30. Jurowska, A.; Szklarzewicz, J.; Hodorowicz, M. Ion Pair Charge-Transfer Salts Based on Protonated Bipyridines and  $[\text{W}(\text{CN})_6(\text{bpy})]^{2-}$  Anion: Structure and Properties. *J. Mol. Struct.* **2022**, *1261*, 132931. [[CrossRef](#)]
31. Sasnovskaya, V.D.; Zorina, L.V.; Simonov, S.V.; Talantsev, A.D.; Yagubskii, E.B.  $[\text{M}^{\text{II}}(\text{H}_2\text{dapsc})]-[\text{Cr}(\text{CN})_6]$  (M = Mn, Co) Chain and Trimer Complexes: Synthesis, Crystal Structure, Non-Covalent Interactions and Magnetic Properties. *Molecules* **2022**, *27*, 8518. [[CrossRef](#)]
32. Etaiw, S.E.H.; Abd El-Aziz, D.M.; Elzeny, I. Nano-Architecture Cobalt (III) Supramolecular Coordination Polymer Based on Host-Guest Recognition as an Effective Catalyst for Phenolic Degradation and Chemical Sensor. *J. Org. Chem.* **2020**, *921*, 121397. [[CrossRef](#)]
33. Peng, H.; Huang, T.; Zou, B.; Tian, Y.; Wang, X.; Guo, Y.; Dong, T.; Yu, Z.; Ding, C.; Yang, F.; et al. Organic-inorganic hybrid manganese bromine single crystal with dual-band photoluminescence from polaronic and bipolaronic excitons. *Nano Energy* **2021**, *87*, 106166. [[CrossRef](#)]
34. Zhang, Y.Q.; Li, M.; Xu, G.C. An In(III)-Based Organic-Inorganic Hybrid Compound  $(\text{C}_3\text{H}_7\text{NH}_3)_3[\text{InCl}_5(\text{H}_2\text{O})]\text{Cl}$  with Dielectric Response Behavior Derived from Order-Disorder Changes of *n*-Propylammonium Cations. *Eur. J. Inorg. Chem.* **2021**, *2021*, 1251–1255. [[CrossRef](#)]

35. Li, M.; Xu, G.C.; Zhang, Y.Q.; Xin, W.-B. Phase Transition, Dielectric Switching Property of an In (III)-Based Organic-Inorganic Hybrid Compound:  $(C_5H_{16}N_2)InBr_5$ . *J. Solid State Chem.* **2020**, *287*, 121329. [[CrossRef](#)]
36. Huang, G.-Z.; Lu, P.-X.; Zeng, M.-M.; Deng, W.; Xie, K.-P.; Wang, Z.-X.; Liu, J.-L.; Chen, Y.-C.; Tong, M.-L. Room Temperature Photochromism and Photoinduced Slow Magnetic Relaxation of Cyanometallic Supramolecular Hybrid Salts. *J. Mater. Chem. C* **2023**, *11*, 5611–5615. [[CrossRef](#)]
37. Huang, C.-R.; Luo, X.-Z.; Liao, W.-Q.; Tang, Y.-Y.; Xiong, R.-G. An Above-Room-Temperature Molecular Ferroelectric:  $[Cyclopentylammonium]_2CdBr_4$ . *Inorg. Chem.* **2020**, *59*, 829–836. [[CrossRef](#)] [[PubMed](#)]
38. Zhao, M.-M.; Zhou, L.; Shi, P.-P.; Zheng, X.; Chen, X.-G.; Gao, J.-X.; Geng, F.-J.; Ye, Q. Halogen substitution effects on optical and electrical properties in 3D molecular perovskites. *Chem. Commun.* **2018**, *54*, 13275. [[CrossRef](#)] [[PubMed](#)]
39. Bala, R.; Sachdeva, D.; Kumar, M.; Prakash, V. Advances in coordination chemistry of hexaurea complexes of chromium (III). *J. Coord. Chem.* **2020**, *73.20–22*, 2801–2837. [[CrossRef](#)]
40. Pechenyuk, S.I.; Zolotarev, A.A.; Gosteva, A.N.; Domonov, D.P.; Shimkin, A.A. Crystal structures and thermal behaviour of double complex compounds incorporating the  $[Cr\{CO(NH_2)_2\}_6]^{3+}$  cation. *J. Mol. Struct.* **2017**, *1147*, 388–396. [[CrossRef](#)]
41. Świetlik, R.; Łapiński, A.; Ouahab, L.; Yakushi, K. Charge ordering in the  $\kappa$ -phase BEDT–TTF salts with  $Co(CN)_6$  and  $Fe(CN)_6$  anions studied by infrared and Raman spectroscopies. *Comptes Rendus Chim.* **2003**, *6*, 395–403. [[CrossRef](#)]
42. Ivanov, V.D. Electrochemical properties of (Co, Fe) CN, cobaltous Prussian blue analogue. *J. Solid State Electrochem.* **2023**, *27*, 2419–2432. [[CrossRef](#)]
43. Shi, C.; Wang, Y.; Han, X.-B.; Zhang, W. Switchable Dielectric Constant in the Cyanometalate-Based Hydrogen-Bonded  $[(CH_3)_2NH_2]_2(H_3O)[Co(CN)_6]$  Framework. *Eur. J. Inorg. Chem.* **2017**, *2017*, 3685–3689.
44. Rok, M.; Moskwa, M.; Hetmańczyk, J.; Hetmańczyk, Ł.; Bator, G. Switchable Dielectric Constant, Structural, and Vibrational Studies of Double Perovskite Organic–Inorganic Hybrids:  $(Azetidinium)_2[KCr(CN)_6]$  and  $(Azetidinium)_2[KFe(CN)_6]$ . *CrystEngComm* **2022**, *24*, 4932–4939. [[CrossRef](#)]
45. Zhang, Y.; Woods, T.; Rauchfuss, T.B. Synthesis and Dynamics of Ferrous Polychalcogenides  $[Fe(E_x)(CN)_2(CO)_2]^{2-}$  ( $E = S, Se, \text{ or } Te$ ). *Inorg. Chem.* **2022**, *61*, 8241–8249. [[CrossRef](#)] [[PubMed](#)]
46. Soto, M.A.; Carta, V.; Cano, M.T.; Andrews, R.J.; Patrick, B.O.; MacLachlan, M.J. Multiresponsive Cyclometalated Crown Ether Bearing a Platinum(II) Metal Center. *Inorg. Chem.* **2021**, *61*, 2999–3006. [[CrossRef](#)]
47. Wang, Z.; Zhang, X.-Y.; Mo, J.-T.; Su, C.-Y.; Pan, M. Ultralong Room-Temperature Phosphorescence from Organic–Inorganic Hybrid Perovskitoid Based on Metal–Organic Complex Component. *Adv. Opt. Mater.* **2023**, *11*, 2203144. [[CrossRef](#)]
48. Wang, Y.; Hu, S.-X.; Cheng, L.; Liang, C.; Yin, X.; Zhang, H.; Li, A.; Sheng, D.; Diwu, J.; Wang, X.; et al. Stabilization of Plutonium(V) within a Crown Ether Inclusion Complex. *CCS Chem.* **2020**, *2*, 425–431. [[CrossRef](#)]
49. Reuter, K.; Thiele, G.; Hafner, T.; Uhlig, F.; von Hänisch, C. Synthesis and Coordination Ability of a Partially Silicon-Based Crown Ether. *Chem. Comm.* **2016**, *52*, 13265–13268. [[CrossRef](#)] [[PubMed](#)]
50. Poe, T.N.; Ramanantoanina, H.; Sperling, J.M.; Wineinger, H.B.; Rotermund, B.M.; Brannon, J.; Bai, Z.; Scheibe, B.; Beck, N.; Long, B.N.; et al. Isolation of a Californium(II) Crown-Ether Complex. *Nat. Chem.* **2023**, *15*, 722–728. [[CrossRef](#)]
51. Ichihashi, K.; Konno, D.; Date, T.; Nishimura, T.; Maryunina, K.Y.; Inoue, K.; Nakaya, T.; Toyoda, K.; Tatewaki, Y.; Akutagawa, T.; et al. Optimizing Lithium Ion Conduction through Crown Ether-Based Cylindrical Channels in  $[Ni(dmit)_2]^-$  Salts. *Chem. Mater.* **2018**, *30*, 7130–7137. [[CrossRef](#)]
52. Huang, Y.; Aierken, A.; Yu, G.; Zhang, W.; Wang, S.; Sui, Y.; Tang, J.; Yang, X.; Zhuang, Y.; Song, Q.; et al. Enhanced Efficiency and Stability of Perovskite Solar Cells Achieved by Incorporating Potassium Cation-18-Crown Ether-6 Complexes. *Org. Electron.* **2023**, *116*, 106766. [[CrossRef](#)]
53. Ma, H.; Luo, D.; Zhao, Q.; Liu, R.; Zhang, Z.; Hou, X.; Sun, X.; Wang, Y. Crown Ether and Crown Ether/ $K^+$  Complex Assisted DOSY NMR: A Versatile Tool for Positional Isomers Identification in Aqueous Solution. *J. Mol. Liq.* **2022**, *345*, 117884. [[CrossRef](#)]
54. Di, F.-F.; Zhou, L.; Chen, W.-J.; Liu, J.-C.; Peng, H.; Tang, S.-Y.; Yu, H.; Liao, W.-Q.; Wang, Z.-X. Room-Temperature Dielectric Switching in a Host–Guest Crown Ether Inclusion Complex. *Inorg. Chem. Front.* **2021**, *8*, 4896–4902. [[CrossRef](#)]
55. Xang, L.; Luo, W.; Yue, Z.-Y.; Huang, Y.-F.; Wang, N.; Miao, L.-P.; Ye, H.-Y.; Shi, C. A New Crown-Ether Clathrate  $[15\text{-Crown-}5][Y(NO_3)_2(H_2O)_5][NO_3]$  with Switchable Dielectric Constant Behavior. *New J. Chem.* **2022**, *46*, 18512–18517. [[CrossRef](#)]
56. Zhang, Z.-X.; Zhang, T.; Shi, P.-P.; Zhang, W.-Y.; Ye, Q.; Fu, D.-W. Exploring high-performance integration in a plastic crystal/film with switching and semiconducting behavior. *Inorg. Chem. Front.* **2020**, *7*, 1239–1249. [[CrossRef](#)]

**Disclaimer/Publisher’s Note:** The statements, opinions and data contained in all publications are solely those of the individual author(s) and contributor(s) and not of MDPI and/or the editor(s). MDPI and/or the editor(s) disclaim responsibility for any injury to people or property resulting from any ideas, methods, instructions or products referred to in the content.